ACS APPLIED ENERGY MATERIALS

Article

A novel ordered rocksalt type Li-rich Li2Ru1-xNixO3-# (0.3 # x # 0.5) cathode material with tunable anionic redox potential

Shiyao Zheng, Feng Zheng, Haodong Liu, Guiming Zhong, Jue Wu, Min Feng, Qi-Hui Wu, Wenhua Zuo, Chaoyu Hong, Yan Chen, Ke An, Ping Liu, Shunqing Wu, and Yong Yang

ACS Appl. Energy Mater., **Just Accepted Manuscript** • DOI: 10.1021/acsaem.9b01051 • Publication Date (Web): 27 Jun 2019

is published by the American Chemical Society. 1155 Sixteenth Street N.W., Washington, DC 20036

A novel ordered rocksalt type Li-rich $Li_2Ru_{1-x}Ni_xO_{3-\delta}$ ($0.3 \leq x \leq 0.5$) cathode material with tunable anionic redox potential

Shiyao Zheng[a], Feng Zheng[b], Haodong Liu[c]*, Guiming Zhong[d], Jue Wu[a], Min Feng[a], Qihui Wu[e], Wenhua Zuo[a], Chaoyu Hong[a], Yan Chen[f], Ke An[f], Ping Liu[c], Shunqing Wu[b]*, Yong Yang[a,g]*

[a]*Collaborative Innovation Center of Chemistry for Energy Materials, State Key Laboratory for Physical Chemistry of Solid Surface, Department of Chemistry, College of Chemistry and Chemical Engineering, Xiamen University, Xiamen, 361005, China*

[b]*Department of Physics, Collaborative Innovation Center for Optoelectronic Semiconductors and Efficient Devices, Key Laboratory of Low Dimensional Condensed Matter Physics (Department of Education of Fujian Province), and Jiujiang Research Institute, Xiamen University, Xiamen 361005, China*

[c]*Department of NanoEngineering, University of California San Diego, La Jolla, California 92093, USA*

[d]*Xiamen Institute of Rare Earth Materials, Haixi Institutes, Chinese Academy of Sciences, Xiamen 361021, China*

[e]*Department of Materials Chemistry, School of Chemical Engineering of Materials Science, Quanzhou Normal University, Quanzhou 362000, China.*

[f]*Neutron Scattering Division, Oak Ridge National Laboratory, Oak Ridge, Tennessee 37830, USA*

[g]*School of Energy, Xiamen University, Xiamen 361005, China*

Email address of corresponding authors: haodong.liu.xmu@gmail.com (Haodong Liu), wsq@xmu.edu.cn (Shunqing Wu), yyang@xmu.edu.cn (Yong Yang)

Abstract

In this work, a series of ordered rocksalt (OR) type Li-rich $Li_2Ru_{1-x}Ni_xO_{3-\delta}$ (LRN_xO, $0.3 \leq x \leq 0.5$) are successfully synthesized and investigated for the first time. X-ray diffraction (XRD) and neutron powder diffraction (NPD) patterns exhibit an obvious phase transition from layered to an OR structure as the Ni content gradually increases from x = 0 to x = 0.5, which leads to different electrochemical behaviors. In the case of OR-$LRN_{0.4}O$, a ~350 mV decrease of the oxygen oxidation potential compared with Li_2RuO_3 (LRO) is observed from around 4.2 V to 3.85 V, which is confirmed by both XPS O 1s spectra and dQ/dV results. The role of Ni substitution on the oxygen redox reaction is studied by first principles calculations, and it is concluded that the formation of the OR-structure caused by Ni substitution is the main reason for lowering the oxygen oxidation potential. In addition, the average discharge voltage of OR-$LRN_{0.4}O$ is also enhanced compared with LRO. This work provides a novel innovative strategy to modulate and control the oxygen anion redox reaction for high-energy-density Li-rich materials, which shed light on the fundamental understanding and optimizing the anion redox process in Li-rich materials.

Key words: cathode materials, Li-rich materials, anionic redox, ordered rocksalt, Ru-based materials

Introduction

Lithium-ion batteries (LIBs) are widely used in electric vehicles, portable electronic devices, and many other applications as energy storage systems at present.[1-3] As the battery technology is becoming more advanced, the demand for Li-ion batteries with higher energy density keeps growing. In order to reach the goal of increasing the energy density of LIBs, both discharge specific capacity and average discharge voltage need to be further improved.[4, 5] From the aspect of capacity, current commercial cathode materials such as $LiCoO_2$, $LiNi_xMn_yCo_{1-x-y}O_2$, $LiFePO_4$, can only deliver practical capacities of around or less than 200 mAh g^{-1}, which cannot suffice the increasing demand on the energy density.[6-9] The reversible capacities of these materials depend on the redox reactions of TM ions. Although the theoretical capacity of $LiCoO_2$ could be achieved by extending the charge cutoff voltage, the capacity is only 270 mAh g^{-1}, and it suffers serious capacity degradation under this cycling condition. Therefore, investigations on new types of cathode materials with high capacities are being carried out.[10-17] The Li-rich materials, which can be generally written as $Li_{1+x}M_{1-x}O_2$, host more Li^+ ions for (de)intercalation compared with traditional commercialized materials, leading to greatly improved theoretical specific capacities (e.g. 460 mAh g^{-1} for Li_2MnO_3). In fact, the actual specific capacity has already reached ~360 mAh g^{-1} according to a recent report by Freire et al.,[14] which suggests Li-rich materials is a promising cathode candidate for next generation LIBs.

The anionic redox reaction plays a significant role in Li-rich materials, which theoretically enables more Li^+ ions beyond the transition metal redox that participate in (de)intercalation process.[18] Nonetheless, this reaction is irreversible in the first cycle of NMC-based Li-rich materials, leading to serious oxygen gas release and the surface transformation.[12] Recently it is reported that Li-rich

materials based on 4d/5d transition metals (TM), such as Ru and Ir, show good reversibility of oxygen redox reaction during charge/discharge process.[19-27] The studies on these model compounds are beneficial for explaining the overall charge compensation mechanism of Li-rich materials. Moreover, the crystal structure and the cation ordering of the Li-rich materials also affect the electrochemical performance and oxygen activity, which is caused by the variation of Li-O-Li configurations and Li^+ diffusion pathways.[28-32]

According to previous reports, the anionic oxidation potential of Li-rich material is generally higher than 4 V so that a high charge cutoff voltage of 4.6 – 4.8 V is required to get the extra capacity from anionic redox process, but cycling a battery at such a high voltage usually causes serious electrolyte decomposition.[33, 34] One solution for avoiding the severe electrolyte degradation at high operating voltage is shifting the oxidation potential of the anions to a lower voltage range, which may also allow higher degree of anionic process take place within the same voltage window. This anion oxidation potential is strongly related to the crystallographic structure of the cathodes according to the studies on layered α-Li_2IrO_3 and 3D-hyperhoneycomb β-Li_2IrO_3 by Tarascon's group, where the O_2^{n-} that represent oxygen oxidation was observed at 3.9 V for α-Li_2IrO_3 and 3.5 V for β-Li_2IrO_3, respectively.[22, 23] As for Ru-based cathodes, the structure of Ni-substituted materials were found to be different from that of other Ru-based ones, but the relationship between the structure and electrochemical properties, especially the oxygen oxidation process, is not fully established.[24, 35] Therefore, we are trying to further explain such an association in this work. Here a series of Ru-based Li-rich materials, for example, Li_2RuO_3 (LRO) and Ni-substituted $Li_2Ru_{1-x}Ni_xO_{3-\delta}$ with a unique ordered rocksalt structure (LRN_xO or LRNO) were successfully synthesized by a facile solid-state method. The crystal structures of the materials were verified by X-ray diffraction (XRD)

and neutron powder diffraction (NPD). With the unique structure, the new ordered rocksalt $LRN_{0.4}O$ displays an oxygen oxidation potential at only around 3.85 V, which was observed from dQ/dV curves and data of X-ray photoelectron spectroscopy (XPS). Density functional theory (DFT) calculations were also conducted to further understand the effects of crystal structure and Li chemical environment on the anionic redox process. In addition, some other electrochemical properties were also studied. The novel OR-$LRN_{0.4}O$ delivers a high discharge capacity of 410 mAh g^{-1} between 1.35 – 4.3 V, and the average discharge voltage is enhanced compared with layered LRO. The combination of *operando* XRD and solid state NMR (ss-NMR) studies confirmed the structural transformation and the evolution of Li^+ local environments during charge/discharge processes, which explained the origin of the high capacity. X-ray absorption near edge structure (XANES) revealed the oxidation states changes of the TM cations. This work controls the anionic oxidation potential through novel electronic and crystal structure design and helps further understanding the oxygen redox mechanism in Li-rich cathode materials.

Experimental section

Material synthesis

A solid-state synthesis was used for synthesizing all the materials (LRO and LRNO). Stoichiometric amounts of Li_2CO_3 (10 wt % excess, Sinopharm Chemical Reagent Co., Ltd. ≥98.0%), NiO (Sinopharm Chemical Reagent Co., Ltd. ≥98.0%) and RuO_2 (Aladdin Industrial Corporation, 99.9%) were firstly grinded and mixed by a mortar and pestle for 10 min and then ball milled at 400 rpm

for 6h with acetone as dispersant via a planetary ball milling machine (QM-3SP04, Nanjing Nanda Instrument Plant). This mixture was then dried and pressed into pellets and was calcined at 950 °C for 15 h in air followed by natural cooling down in the furnace. The samples were stored in an Ar-filled glove box before characterization or electrochemical test to avoid the moisture and air contamination.

Electrochemical tests

All electrochemical tests were conducted in CR2025 coin-type cells. The cells were assembled in an argon-filled glove box, using Li discs as the negative electrode. The active material, acetylene black (AB) and poly(-vinylidene fluoride) binder (PVDF) were ball milled in a weight ratio of 8:1:1 in N-methyl-2-pyrrolidene (NMP) solvent to obtain the slurry, which was then cast on an aluminum foil and used as the positive electrode. 1 M $LiPF_6$/EC-DMC (1:1 by vol.) (Shenzhen CAPCHEM Co., Ltd. (China)) were used as the electrolyte. Galvanostatic tests were performed on a LAND CT-2001A (Wuhan, China) battery test system.

Material characterization

The powder XRD patterns were recorded with a Rigaku Ultima IV powder X-ray diffractometer using Cu Kα radiation (λ = 1.5406 Å). Time-of-flight (TOF) powder neutron diffraction data were collected at the VULCAN instrument at Spallation Neutron Sources (SNS), Oak Ridge National Laboratory (ORNL).[36] Approximately 1.6 g of powder was filled into a vanadium sample can. An

incident beam (5mm×12mm) allowing 0.5~3.6 Å d-space in the diffracted pattern of the ±90° 2θ detector banks, was selected using the double-disk choppers at 20 Hz frequency. High-resolution mode was employed with Δd/d ~0.25%. The SNS was at nominal, 1100KW, power.[36] Powder neutron diffraction data were collected in high resolution mode for a duration of 3 h and processed using VDRIVE software.[37] Rietveld refinement against the neutron diffraction was performed using General Structure Analysis System (GSAS) software with EXPGUI interface[38, 39] to obtain the lattice and atomic parameters of the powder samples. Schematic diagrams of $LRN_{0.4}O$ and LRO were drawn by a VESTA software.[40]

Operando X-ray diffraction patterns of LRNO were collected using beamline BL14B1 at the Shanghai Synchrotron Radiation Facility (SSRF) (Shanghai, China) with a wavelength of 0.6887 Å.[41] The *operando* XRD data were collected by a linear position sensitive silicon detector (MYTHEN 1K) with exposure time of ~60 s/step. A standard CeO_2 powder sample was used for calibration. The current density used in the experiment was 80 mA g^{-1} and the voltage range was 1.25 - 4.6V. The *ex-situ* and *in-situ* XANES data at the Ni and Ru K-edges were collected in transmission mode at a room temperature, using ion chamber detectors at beamline BL14W1 of the SSRF and Si(111)/Si(311) double-crystal monochromators.[42] The focal spot size at the position of the sample was ~0.25 mm. The monochromators were calibrated to reject higher harmonics of the selected wavelength (harmonic content < 10^{-4}) and data was collected over a range of energies, from 200 eV below to 800 eV above the Ni (8333 eV) and Ru (22117 eV) K-edges. The incident photon energy was calibrated using standard Ni and Ru metal foils just prior to data collection in all *ex-situ* XAFS measurements. Processing and fitting of the XAFS data were performed using an Athena software.[43]

All ss-NMR experiments were performed in a 14.1 T magnetic field with a Bruker Avance III 600 spectrometer, operating at a ^{7}Li resonance frequency of 155.5 MHz, using 1.3 mm probe-heads at a magic-angle spinning (MAS) frequency of 60 kHz. A recycle delay of 0.05 s and a 90° pulse length of 1.8 μs were used for ^{7}Li. The ^{7}Li spectra were obtained with a stepwise spin-echo pulse sequence. The irradiation frequency of ^{7}Li was varied with a step size of 0.12 MHz. A projection-magic angle turning phase-alternating spinning sideband (pj-MATPASS) pulse sequence was also applied in order to acquire isotropic ^{7}Li NMR spectra. The chemical shifts of ^{7}Li were referenced to LiCl solution (0 ppm).

XPS measurements were carried out in an ultrahigh vacuum system using monochromatized Al Kα radiation (1486.6 eV) and an Omicron Sphera II hemispherical electron energy analyzer. The binding energies were calibrated by setting the hydrocarbon C 1s (C−C, C−H) signal to 284.8 eV. A sample holder with all the electrodes to be measured was placed into a sealed argon-filled container, which was directly connected to the XPS spectrometer afterwards so that all the samples are transferred without exposure to the air.

First Principles Calculations

The present calculations are carried out by using the projector-augmented wave (PAW)[44] representations within the spin-polarized density functional theory (DFT) method, as implemented in the Vienna *Ab initio* Simulation Package (VASP).[45, 46] The Perdew-Burke-Ernzerhof (PBE)[47] exchange-correlation functional is used, together with the Hubbard U corrections (GGA + U) in the rotationally invariant form introduced by Dudarev *et al.*[48] to address the self-interaction energy. In

this work, an effective single parameter *U-J* is set to 4 and 6 eV for Ru and Ni, respectively.[28] The wave functions are expanded by using the plane waves up to a kinetic energy cutoff of 500 eV. Brillouin-zone integrations are approximated by using special *k*-point sampling of Monkhorst-Pack scheme[49] with a *k*-point mesh resolution of $2\pi \times 0.02$ Å^{-1}. The unit cell lattice vectors (both the unit cell shape and size) are fully relaxed together with the atomic coordinated until the force on each atom is less than 0.01 eV/Å.

Results and discussions

XRD and NPD studies on crystal structure of LRO and LRNO

A series of XRD patterns of the as-prepared LRO and LRNO are presented in **Fig. 1a**. The structure of LRO is indexed to a layered structure with monoclinic C2/c space group, which is consistent with previous works.[20, 25] As the amount of Ni increases, obvious changes of the diffraction peaks are observed. The superstructure peaks between 20° and 30°, which indicate an ordering of LiM_6 units in the TM layers of layered oxides,[20, 50, 51] disappear in the high Ni content LRNO materials ($x \geq 0.3$). **Fig. 1b** displays the magnified regions of certain diffraction peaks in **Fig. 1a**, which clearly demonstrates the phase transformation from monoclinic structure to another phase after the Ni-substitution.

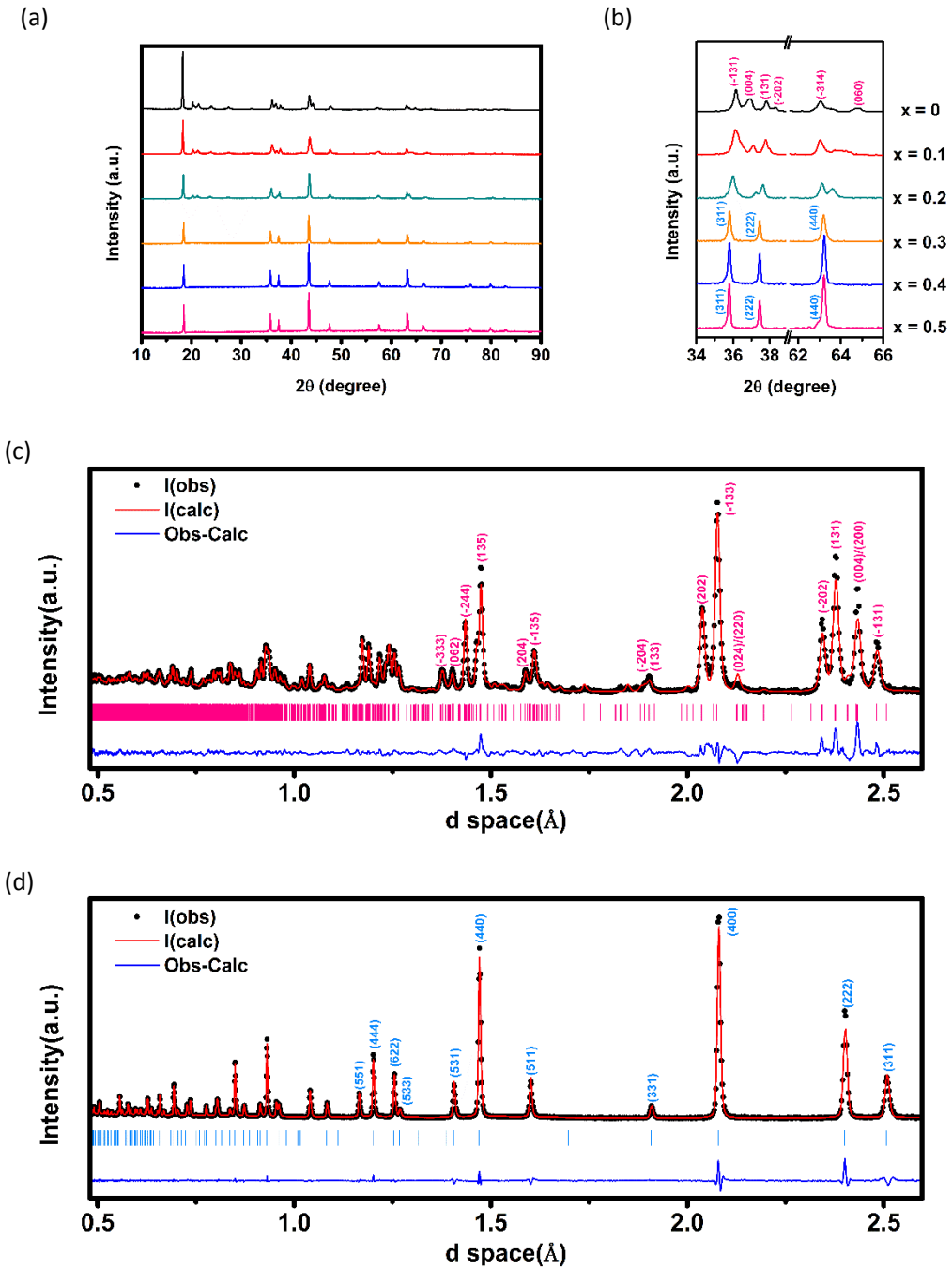

Fig. 1 Structural analysis of LRO and LRNO. a) XRD patterns of LRO and LRNO. b) Details of certain diffraction peaks in Fig. 1a. c) d) NPD patterns of LRO and $LRN_{0.4}O$, respectively. Notes and bars in pink and cyan represent layered and OR structure, respectively.

In contrast to the small X-ray scattering cross-sections of light elements, such as Li and O in, neutron diffraction has better sensitivity to the site occupancy and the atomic displacement of both light

elements and transition metal elements in the crystal structure.[52, 53] Rietveld refinement on the NPD patterns of the LRO and LRNO was conducted to quantitatively analyze their crystal structures.[54, 55] **Table 1** lists the lattice parameters of the materials with different Ni content. The LRO material possesses a layered structure with C2/c space group. When x in $LRN_xO \geq 0.3$, the NPD pattern is indexed to an ordered rocksalt (OR) structure with a cubic $Fd\bar{3}m$ space group.[56] The $LRN_{0.1}O$ and $LRN_{0.2}O$ show coexistence of both phases.

Table 1. Lattice Parameters Calculated from Rietveld Refinement of NPD Data of Pristine LRO and LRNO with Various Ni Contents

Ni content			0	0.1	0.2	0.3	0.4	0.5
Layered structure (C2/c)	Lattice parameters	*a*	4.9347(3)	4.9805(7)	5.0599(6)			
		b	8.7775(7)	8.7659(13)	8.7408(9)			
		c	9.8800(8)	9.8544(14)	9.8010(9)			
		β	100.020(5)	99.940(8)	99.777(10)			
	Mass content (%)		100	75.4	31.8	0	0	0
OR structure ($Fd\bar{3}m$)	Lattice parameter *a*			8.2939(19)	8.3018(7)	8.3074(5)	8.3154(1)	8.3148(2)
	Mass content (%)		0	24.6	68.2	100	100	100
R_{wp} (%)			6.68	6.66	5.10	7.81	3.65	3.78

Fig. 1c and **Fig. 1d** shows the NPD patterns and Rietveld refinement of LRO and $LRN_{0.4}O$. **Table**

2 displays the atomic structure parameters of $LRN_{0.4}O$ calculated from NPD data by GSAS as an example to describe the OR structure. All the NPD patterns and Rietveld refinement results of materials with other compositions are available in supporting information. (**Fig. S1** and **Table S1**) The $Fd\bar{3}m$ space group is often associated with the spinel materials in LIBs,[57] and the frameworks of the OR-$LRN_{0.4}O$ and spinel materials are indeed quite similar. Due to the differences on the specific sites and occupancy of the Li ions, these two structures are not exactly the same. For instance, all the Li ions are located in 8a tetrahedral sites in the spinel material $LiMn_2O_4$,[58] while the Li ions stays in both 16c and 16d octahedral sites in $LRN_{0.4}O$. Since the $LRN_{0.4}O$ is Li-rich, it is not hard to understand that the excess Li^+ ions sits in the 16d sites. Based on the description above, this Ni substituted LRO is a cation-ordered rocksalt instead of a cation-disordered rocksalt structure (space group: $Fm\bar{3}m$), and the name of ordered rocksalt here is just for the convenience of classification.[56] **Fig. 2a** presents the crystal structure of Li-rich LRO, which exhibits 2D Li diffusion pathways. As a comparison, **Fig. 2b** and **2c** illustrating the 3D Li diffusion $LRN_{0.4}O$ is given. The facts of Li/Ni mixing and oxygen defects are also presented in **Table 2**. Some Ni ions exchange their position with Li ions in 16c sites, and the site occupancy factors (S.O.F.) of oxygen is less than 1, which indicates the existence of oxygen vacancies. The oxygen deficiency is caused by substituting the Ru by low oxidation states Ni into the structure. For example, when the valence of M in $Li_2MO_{3-\delta}$ equals +4, there is no oxygen vacancy in the structure. Since the Ni oxidation state is less than +4, when $x > 0$, the δ in $Li_2Ru_{1-x}Ni_xO_{3-\delta}$ has to be more than 0 as well. This phenomenon was also noticed by Satish et al in $Li_2Ru_{0.75}Fe_{0.25}O_{3-\delta}$.[59]

Table 2. Atomic Structure Parameters of OR-$LRN_{0.4}O$ Calculated from Rietveld Refinement.

Atom	Wyckoff site	x	y	z	Occupation factor	Uiso
Li1	16c	0	0	0	0.950(3)	0.02443
Li2	16d	1/2	1/2	1/2	0.383(3)	0.00553
Ru	16d	1/2	1/2	1/2	0.4	0.00553
Ni1	16d	1/2	1/2	1/2	0.211(3)	0.00553
Ni2	16c	0	0	0	0.050(3)	0.02443
O	32e	0.2560(1)	0.2560(1)	0.2560(1)	0.869(9)	0.01088

Electrochemical Performances

Fig. 3a and Fig. 3b compares the first charge/discharge voltage profiles and dQ/dV curves of LRO and LRNO within the voltage window of 2−4.6 V, at 50 mA g^{-1}. The specific capacities of LRN_xO are all around 250 mA g^{-1} for $0 \leq x \leq 0.4$, and diminish a little for $LRN_{0.5}O$. From dQ/dV curves, apparent peak shifts are observed. The peak of LRO at ~4.27 V during charge represents the oxidation of oxygen,[19-21, 25] which gradually moves to lower than 4 V from LRO to $LRN_{0.5}O$. On the other hand, the discharge peak at 3.3 V moves up to ~3.7 V with the increase of Ni content, indicating the enhancement of average discharge voltage. A comparison of the initial discharge curves between LRO and $LRN_{0.4}O$ and the average voltages of the first discharge process for all LRO and LRNO are presented in **Fig. S2**. The results imply that the materials with higher average discharge voltages are obtained by Ni-substitution. The $LRN_{0.4}O$ exhibits an enhanced average discharge voltage of 3.47 V, which is ~210 mV higher than the LRO. It's not logical if the oxygen

oxidation potential is lowered while the corresponding oxygen reduction potential is raised, so this enhanced discharge voltage should be attributed to the variation of phase transformation and TM reduction potential after Ni-substitution. The oxidation peak shift of LRO at 3.4 V and 3.7 V to higher potentials as the amount of Ni increases in dQ/dV curves should also be noticed (**Fig. 3b**), which implies TM oxidation.

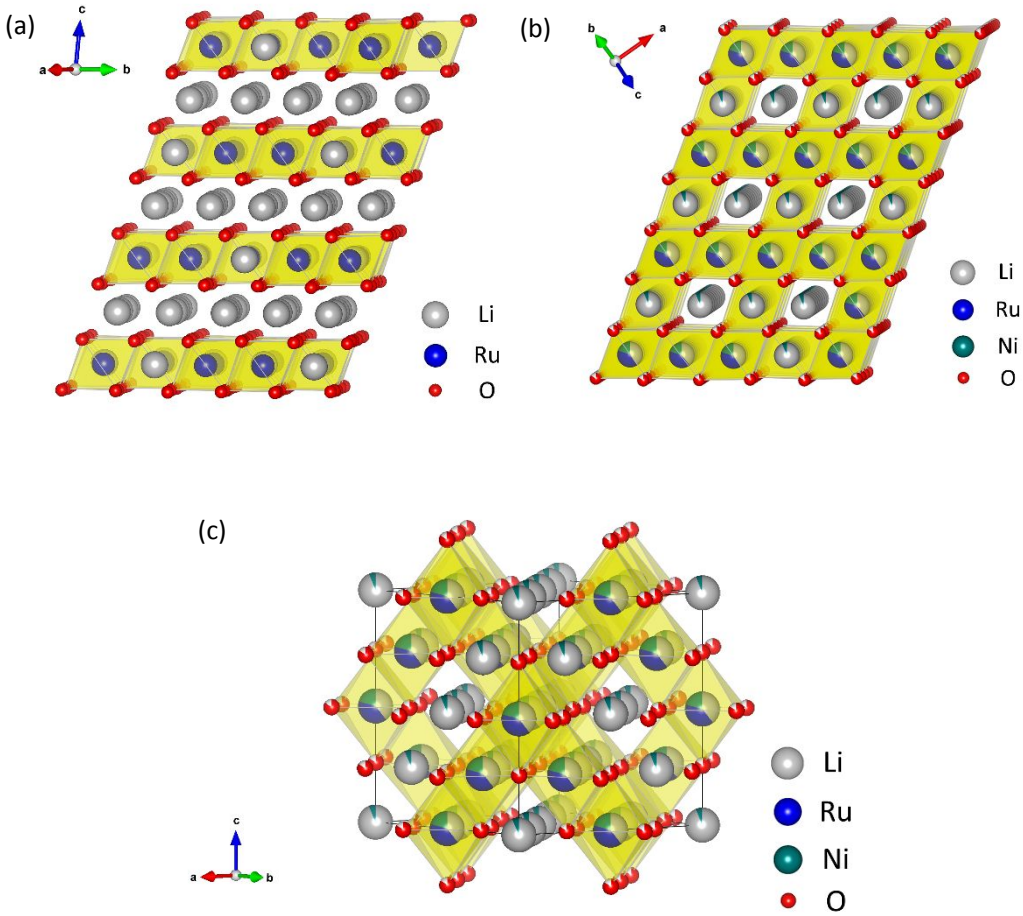

Fig. 2 Schematic diagram of a) LRO with a layered structure b) $LRN_{0.4}O$ with an OR structure c) a cubic unit cell of OR-$LRN_{0.4}O$.

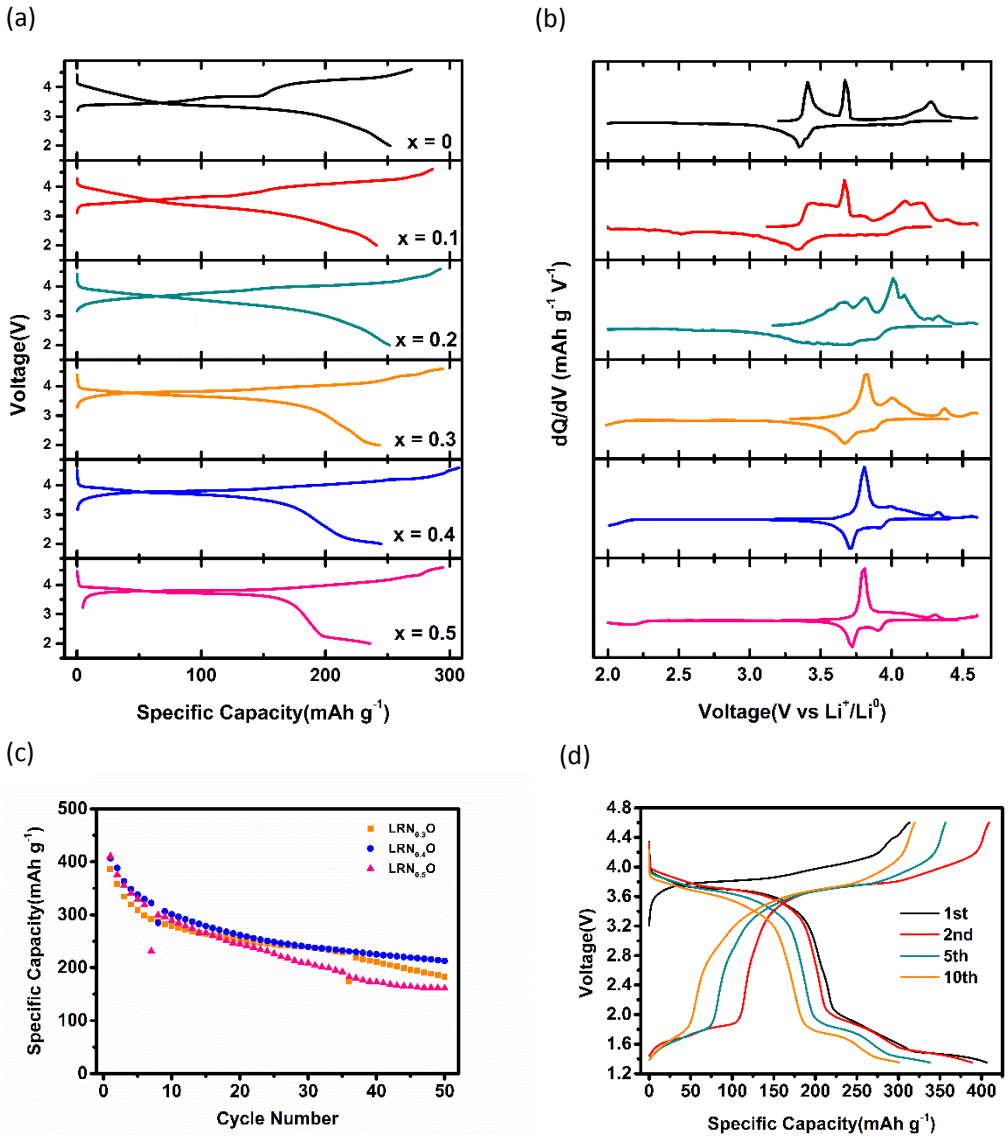

Fig. 3 Electrochemical performances of LRO and LRNO. a) b) First cycle charge/discharge voltage profiles and corresponding dQ/dV curves between 2.0−4.6 V at 50 mA g^{-1}. c) Comparison of specific capacities among $LRN_{0.3}O$, $LRN_{0.4}O$ and $LRN_{0.5}O$ over the course of 50 cycles between 1.35−4.6 V at 50 mA g^{-1} and d) Voltage profiles of $LRN_{0.4}O$ between 1.35−4.6 V at 50 mA g^{-1}.

When $x \geq 0.3$, a new discharge plateau below 2.3 V occurs, which becomes more evident as the Ni content increases. Due to the limitation of cutoff discharge voltage, this plateau is not completely

shown. In order to fully understand the electrochemical behaviors of the material, especially the plateau at low voltage region, the voltage window was further extended to 1.35 – 4.6 V.[23, 60, 61] The comparison of capacities of $LRN_{0.3}O$, $LRN_{0.4}O$ and $LRN_{0.5}O$ over the course of 50 cycles are given in **Fig. 3c**. The specific capacities of all the materials at the first discharge exceed 400 mAh g^{-1}, and the Li-rich $LRN_{0.4}O$ shows the best stability. Therefore, $LRN_{0.4}O$ is chosen for further characterizations. **Fig. 3d** exhibits the voltage profile of $LRN_{0.4}O$, which delivers a high specific capacity of 410 mAh g^{-1} at the first discharge process. This equals to an exchange of 2.14 e^- per mole of $LRN_{0.4}O$. Here the discharge plateaus below around 2.0 V are completely exhibited, which implies Li in tetrahedral sites.[60, 62] According to **Fig. 3d**, the capacity fading of the first 10 cycles is 105 mAh g^{-1}, which contains 48 mAh g^{-1} above 2.0 V and 57 mAh g^{-1} below 2.0 V. Therefore, the capacity fading should be ascribed to the electrochemical redox reactions both above 2.0 V and below 2.0 V. In addition, the first and the second charge curves above 3.2 V have similar shapes, unlike the majority of other Li-rich materials. This phenomenon implies that the oxygen redox is not to an excessive extent.[10]

Operando XRD measurement

An *operando* XRD experiment on $LRN_{0.4}O$ was conducted for real time observation of the phase transformations during the initial charge/discharge processes. The electrochemical voltage profile and XRD patterns are depicted in **Fig. 4a**. For the convenience of analysis, all data are divided into four regions. The first region is before 3.8 V during the charge. The $LRN_{0.4}O$ maintains the rocksalt phase without obviously structural change in this region (OR phase 1). The second region contains

the rest of the charge. In this region, several new diffraction peaks start to appear, which can be indexed to a layered structure with a space group of R$\bar{3}$m. The XRD pattern at 4.6 V is plotted in **Fig. S3**, the observed new phase is consistent with the structure of a delithiated layered $LiNiO_2$.[63] The third region is from the beginning of discharge to 1.6 V. Both of the cubic rocksalt phase and layered phase exist in the $LRN_{0.4}O$. At the end of this region, the newly formed layered phase almost vanishes, only the initial ordered rocksalt structure stays. In the fourth region, some new diffraction peaks start to emerge closely to the pristine peaks at the lower angle side, which can be also indexed to an Fd$\bar{3}$m space group with larger lattice parameters (OR phase 2). At the end of discharge, another new peak grows at a very low angle of ~7.85°, which implies that the material is overlithiated. It should be noticed that the original peaks from ordered rocksalt phase exist throughout the whole charge/discharge process without obvious shift, which is different from other types of Li-rich materials such as the Ru-based layered oxides,[20, 25] 3d metal-based materials[64] and cation disordered rocksalt type cathodes.[29] The zero shifting of the ordered rocksalt peaks suggest great stability of the main framework. **Fig. 4b** illustrates the calculated lattice parameters of different phases during the electrochemical cycling. The lattice parameter of the pristine OR main phase keeps stable, and the volume change of the layered phase is less than 2.5%. Below 1.6 V during discharge, the lattice parameter of newly formed OR phase enlarged by 10% compared with pristine phase. At the very end of discharge process, the lattice parameter of the overlithiated phase becomes much larger. It is not easy to judge the structure merely by the single new diffraction peak at ~7.85° for the overlithiated phase in **Fig. 4a**, and here the lattice parameter was calculated according to Fd$\bar{3}$m space group for the convenience of comparison, which should be mentioned.

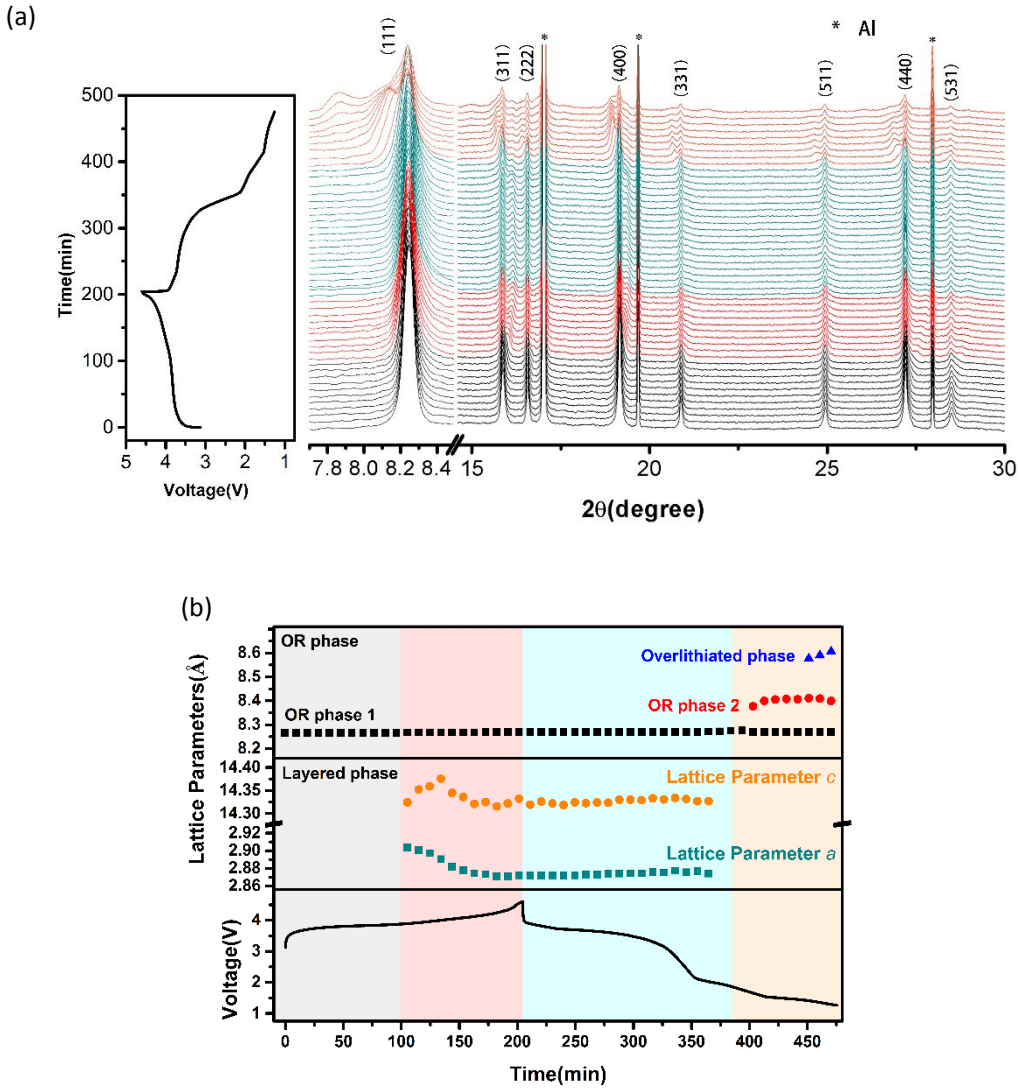

Fig. 4 a) *Operando* XRD patterns of $LRN_{0.4}O$ during its first cycle between 1.25 – 4.6 V at current density of 80 mA g^{-1}. b) Corresponding Lattice parameters of different phases calculated from XRD.

^{7}Li Solid-state NMR Spectra

The new discharge plateau below 2.3 V in $LRN_{0.4}O$ is associated with the new phase formation, which is verified by the *Operando* XRD. However, the specific sites of the extra Li ions that inserts into the $LRN_{0.4}O$ during the low voltage discharge region cannot be identified by XRD. Solid-state

NMR experiments were performed on the $LRN_{0.4}O$ to further identify the chemical environment of Li ions at different states of (dis)charges. **Fig. 5** displays the resulting ^{7}Li spin-echo *ex-situ* NMR spectra. For all the spectra, broad peaks show the information of Li in the sample and sharp ones with asterisk are ascribed to impurity peaks of 0 ppm and their sidebands. During the charge process, the sample peak keeps moving close towards 0 ppm, which is due to the oxidation of TM cations adjacent to Li and thus the decrease of the number of unpaired electron. Next, the broad peak in the 2.15 V discharge spectra shifts back, indicating a reversible (de)lithiation process from pristine to the 2.15 V discharge state. In the subsequent discharge process, the peak moves towards an even lower chemical shift, which confirms that tetrahedral sites are really being occupied by Li ions.[65]

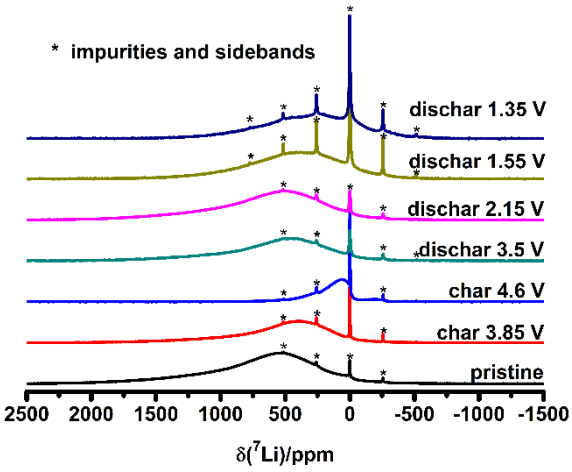

Fig. 5 ^{7}Li spin-echo *ex-situ* NMR spectra. In all spectra, the sharp peaks marked with asterisks at 0 ppm and other positions represent Li-containing impurities, such as LiF and Li_2CO_3, and their sidebands, respectively.

Oxidation State Analysis

The oxidation states of TM cation and oxygen were characterized by XAS and XPS for completely understanding the charge compensation mechanism during the whole charge/discharge process. The variation of the TM cation oxidation state was firstly studied by XANES. *Ex-situ* XANES spectra at the Ni K-edge of $LRN_{0.4}O$ at different states of charges are given in **Fig. 6a**. Compared with the spectrum of NiO, the oxidation state of Ni in the pristine $LRN_{0.4}O$ is higher than +2. With the help of Ni 2p XPS spectra of the pristine electrode displayed in **Fig. S4**, the valence state of Ni on the surface of $LRN_{0.4}O$ can be quantitatively clarified.[66, 67] The fitting results show that the relative content of Ni^{2+} and Ni^{3+} on the $LRN_{0.4}O$ particle surface are 17.1% and 82.9%, respectively. During the charge process, the absorption edge keeps shifting towards higher energy, implying an evolution from Ni^{2+}/Ni^{3+} to Ni^{4+}. On the other hand, **Fig. 6b** shows *in-situ* Ru K-edge spectra upon charging, where an oxidation process from Ru^{4+} to Ru^{5+} occurs from OCV to 4 V, and no further oxidation afterwards. It should be also noticed that the pre-edge peak exists even at the OCV state, which is associated with the oxygen defect in the as-prepared LRNO material mentioned above. Moreover, beyond 3.8 V during charge, the pre-edge peak keeps increasing, which implies the distortion of RuO_6 octahedral and a lowered oxygen oxidation potential at only around 3.85 V.[60]

Ex-situ XPS analysis was also carried out for studying oxygen redox reaction. **Fig. 6c** shows *ex-situ* O 1s XPS spectra during the first cycle. In the spectrum for the pristine material, two profile peaks at ~529.5 eV and ~531.8 eV are observed, which are related to O^{2-} in the lattice and weakly adsorbed oxygen species.[20, 68, 69] During delithiation process, some oxidation products of electrolyte at ~533.5 eV can be found. At 3.85 V charge state, a new profile peak occurs, which represents the oxidized lattice oxygen O_2^{n-} ($1 \leq n \leq 3$). It is worth noting that the anionic oxidation reaction in this novel ordered rocksalt $LRN_{0.4}O$ occurs at a much lower potential than other reported Ru-based

systems with the Li/M ratio = 2 : 1, where the anionic oxidation reaction can only be achieved above 4 V.[19-21] This unique property also matches the dQ/dV curve mentioned above in **Fig. 3b** and the pre-edge peaks in Ru XANES spectra. As a consequence, the lowered anionic oxidation potential is beneficial for operating the Li-rich materials within a safe electrolyte voltage range without sacrificing the high capacity.[34, 69] In previous reports of layered α-Li_2IrO_3 and 3D-hyperhoneycomb β-Li_2IrO_3, the lowered oxygen oxidation potentials are also observed at around 3.9 V and even 3.5 V, respectively.[22, 23] These facts all imply that the oxygen oxidation should be strongly linked with the selection of TM cations and the crystal structure, which is discussed in first principles calculations in detail.

(a) (b)

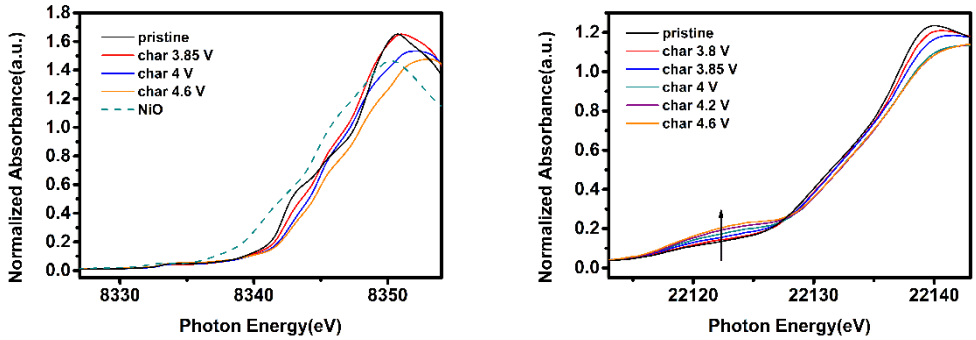

(c)

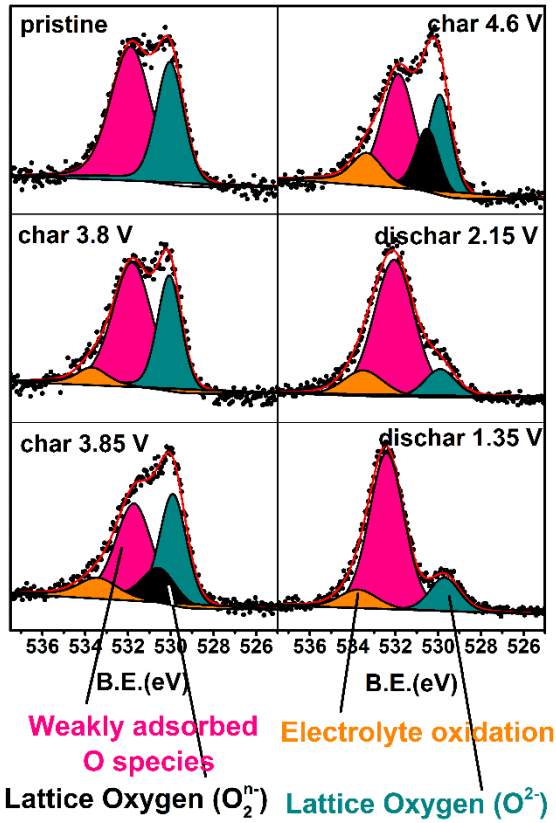

Fig. 6 Oxidation state analysis. a) *Ex-situ* XANES spectra at the Ni K-edge of $LRN_{0.4}O$ at different states of charges. b) *In-situ* XANES spectra at the Ru K-edge of $LRN_{0.4}O$ upon charging. c) *Ex-situ* O 1s XPS spectra during the first cycle at different states of charges.

First Principles Calculations

As mentioned above, the anionic oxidation reaction of $LRN_{0.4}O$ below 4 V was observed by electrochemical analysis, Ru XAS pre-edges, and O 1s XPS. However, the exact role of Ni on the local oxygen environment and electronic structure of oxygen has not been identified yet. The DFT calculations were carried out to further understand the fundamental reasons of oxygen oxidation potential change in LRNO. Based on the structural parameters from the diffraction data, a

$1 \times 1 \times 3$ conventional cell of $Li_{64}Ru_{19}Ni_{13}O_{96}$ (~$32Li_2Ru_{0.6}Ni_{0.4}O_3$) polymorph with 32 formula unites is constructed **(Fig. S5)**, where oxygen defects and Li/Ni mixing between 16c and 16d sites are not considered at the beginning. Here Li, Ru and Ni atoms are randomly distributed in 16d sites and there is only Li in 16c sites. The calculated and experimental XRD patterns are displayed in **Fig. S6**, which reveals that the calculated XRD pattern of OR-LRNO under relaxation is highly consistent with the experimental result.

In layered Li_2RuO_3 (LRO), there is only one local oxygen environment, in which each oxygen atom is coordinated by four Li and two Ru (marked as 4Li/2Ru, **Fig. 7a**). By contrast, in the OR-LRNO structure, each O are connected with three atoms in 16c sites (all are Li regardless of Li/Ni mixing) and three in 16d sites (random distribution of Li, Ru and Ni), therefore, the number of Li for coordination can be 3, 4, 5 or 6, leading to 10 possible local environments including 4Li/2Ru. To explain the modified oxygen oxidation in OR-LRNO, we compared the projected density of states (pDOS) of oxygen 2*p* states of different oxygen configurations between OR-LRNO and layered LRO. Three types of local environment in OR-LRNO were firstly considered: 1) oxygen surrounded with four Li and two Ru (also marked as 4Li/2Ru, but for LRNO, **Fig. 7b**), 2) oxygen surrounded with four Li, one Ru and one Ni (marked as 4Li/Ru/Ni, **Fig. 7c**), and 3) five Li and one Ru (marked as 5Li/Ru, **Fig. 7d**). The pDOS of the oxygen 2*p* states in 5Li/Ru is much closer to the Fermi level than that with other configurations (**Fig 7a-c**). The contribution of pDOS near the Fermi level is largely affected by the M-O orbital interactions. Here 'M' refers to Li, Ni and Ru, and the orbital interaction is Li-O < Ni-O < Ru-O.[70] For 5Li/Ru, it can be regarded as one Ru substituted by Li in 4Li/2Ru configuration. The weaker interaction leads to the increasing oxygen pDOS below the Fermi level, which suggests a much easier oxygen oxidation process. Based on this result, if there

are more than 4 Li connecting to oxygen, the pDOS of oxygen will move up to higher energies (**Fig. S7a-d**). Conversely, the oxygen pDOS will be away from the Fermi level if one Li is substituted by Ni or Ru in 4Li/2Ru (3Li/2Ru/Ni and 3Li/3Ru, **Fig. S8a-c**). For the last two configurations, if one Li and one Ru are substituted by two Ni in 4Li/2Ru, the effect on oxygen 2*p* states may cancel out, as the variation of oxygen pDOS is not obvious near the Fermi level (3Li/Ru/2Ni, **Fig. S9b**). Moreover, if one more Ru is replaced by Ni (3Li/3Ni, **Fig. S9c**), the energy of oxygen pDOS will be higher than that in 4Li/2Ru.

According to the discussions above, several oxygen environments in OR-LRNO, especially oxygen connected with more than 4Li, have higher energies of O 2*p* orbitals than that 4Li/2Ru in layered LRO. The reason can be explained as follows: (1) The main reason is, unlike layered LRO which exhibits only one local oxygen environment, a variety of oxygen configurations exist in OR-LRNO due to the random distribution of Li, Ru and Ni in 16d sites. Therefore, oxygen are possible to coordinate with more Li, leading to higher energies of O 2*p* states. (2) Ni substitution of LRO itself can also bring the weaker Ni-O than original Ru-O, which can make O 2*p* states more closed to the Fermi level. This is the secondary reason. As shown in **Fig. 7e**, the total oxygen density of states (DOS) of OR-LRNO is closer to the Fermi level than that of layered LRO, and the difference is exhibited in orange. These results explain the lower oxygen oxidation potential that are observed in Ni-substituted LRNO materials. Finally, the oxygen defects and Li/Ni mixing are also considered, the total DOS of $Li_{64}Ru_{19}Ni_{13}O_{84}$ supercell with 0.875 oxygen defects (random distribution of O defects) of OR-LRNO (**Fig. S10**) doesn't show much difference compared with OR-LRNO without O defects and Li/Ni mixing, indicating that O defects and Li/Ni mixing have little effect on oxygen oxidation potential.

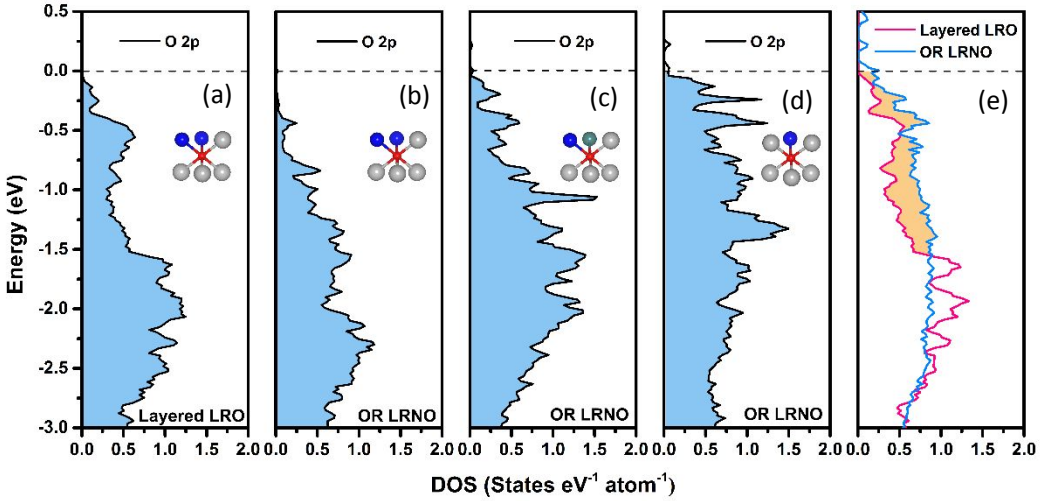

Fig. 7 a) b) c) PDOS of the O 2p orbitals in different local environments. a) 4Li/2Ru in layered LRO, b) 4Li/2Ru, c) 4Li/Ru/Ni and d) 5Li/Ru in OR-LRNO. Li, Ru, Ni and O are colored in grey, blue, dark cyan and red, respectively. e) Total DOS of O in layer LRO (pink) and OR-LRNO (cyan). Orange area shows the differences of DOS of Oxygen in LRO and LRNO closely below the Fermi level.

Conclusions

In conclusion, a series of new ordered rocksalt type LRN_xO ($0.3 \leq x \leq 0.5$) are obtained by the facile solid-state synthesis. The oxygen oxidation reaction of $LRN_{0.4}O$ occurs at a low potential of around 3.85 V during charge process, which has never been observed in other type of Ru-based Li-rich materials before. This phenomenon can be mainly attributed to the formation of OR-structure after Ni-substitution according to the DFT calculation. The new material shows exceptionally a high discharge capacity of 410 mA h g^1 in the voltage range of 1.35 – 4.6 V, with a high average discharge

voltage of 3.47 V in the voltage range of 2 - 4.6 V. This study paves a new way to lower the potential of oxygen oxidation by simple Ni-substitution, which is beneficial for achieving high capacity and safe Li ion batteries. Although Ru is expensive, this work mainly focus on the fundamental understanding on manipulating the oxygen behaviors, which provides a new possibility – some other low-cost elements might be used to replace Ru for high energy density Li-rich materials with an OR structure.

Acknowledgement

This work was financially supported by the National Natural Science Foundation of China (Grant Nos. 21761132030, 21428303, and 21621091) and the National Key Research and Development Program of China (Grant Nos. 2018YFB0905400 and 2016YFB0901500).

This manuscript has been authored by UT-Battelle, LLC under Contract No. DE-AC05-00OR22725 with the U.S. Department of Energy. The United States Government retains and the publisher, by accepting the article for publication, acknowledges that the United States Government retains a non-exclusive, paid-up, irrevocable, worldwide license to publish or reproduce the published form of this manuscript, or allow others to do so, for United States Government purposes. The Department of Energy will provide public access to these results of federally sponsored research in accordance with the DOE Public Access Plan (http://energy.gov/downloads/doe-public-access-plan).

Neutron diffraction work was carried out at the Spallation Neutron Source (SNS), which is the U.S.

Department of Energy (DOE) user facility at the Oak Ridge National Laboratory, sponsored by the Scientific User Facilities Division, Office of Basic Energy Sciences. The authors thank Mr. M. J. Frost at SNS for the technique support. The authors also thank beamlines BL14B1 and BL14W1 of SSRF (Shanghai Synchrotron Radiation Facility) for providing beam time.

References

[1] Assat, G., Tarascon, J.-M. Fundamental understanding and practical challenges of anionic redox activity in Li-ion batteries. *Nature Energy*. 2018;3(5):373-386.

[2] Etacheri, V., Marom, R., Elazari, R., Salitra, G., Aurbach, D. Challenges in the development of advanced Li-ion batteries: a review. *Energ Environ Sci*. 2011;4(9):3243-3262.

[3] Wang, L., Chen, B., Ma, J., Cui, G., Chen, L. Reviving lithium cobalt oxide-based lithium secondary batteries-toward a higher energy density. *Chemical Society Reviews*. 2018;47(17):6505-6602.

[4] Wang, S.H., Li, Y.X., Wu, J., Zheng, B.Z., McDonald, M.J., Yang, Y. Toward a stabilized lattice framework and surface structure of layered lithium-rich cathode materials with Ti modification. *Phys Chem Chem Phys*. 2015;17(15):10151-10159.

[5] Huang, X.K., Zhang, Q.S., Gan, J.L., Chang, H.T., Yang, Y. Hydrothermal Synthesis of a Nanosized LiNi0.5Mn1.5O4 Cathode Material for High Power Lithium-Ion Batteries. *Journal of the Electrochemical Society*. 2011;158(2):A139-A145.

[6] Ji, Y., Zhang, P., Lin, M., Zhao, W., Zhang, Z., Zhao, Y., Yang, Y. Toward a stable electrochemical interphase with enhanced safety on high-voltage LiCoO2 cathode: A case of phosphazene additives. *J Power Sources*. 2017;359:391-399.

[7] Liu, H., Strobridge, F.C., Borkiewicz, O.J., Wiaderek, K.M., Chapman, K.W., Chupas, P.J., Grey, C.P. Capturing metastable structures during high-rate cycling of LiFePO4 nanoparticle electrodes. *Science*. 2014;344(6191).

[8] Chen, Z., Chao, D., Liu, J., Copley, M., Lin, J., Shen, Z., Kim, G.-T., Passerini, S. 1D nanobar-like LiNi0.4Co0.2Mn0.4O2 as a stable cathode material for lithium-ion batteries with superior long-term capacity retention and high rate capability. *J Mater Chem A*. 2017;5(30):15669-15675.

[9] Zheng, S., Hong, C., Guan, X., Xiang, Y., Liu, X., Xu, G.-L., Liu, R., Zhong, G., Zheng, F., Li, Y., Zhang, X., Ren, Y., Chen, Z., Amine, K., Yang, Y. Correlation between long range and local structural changes in Ni-rich layered materials during charge and discharge process. *J Power Sources*. 2019;412:336-343.

[10] Lee, J., Kitchaev, D.A., Kwon, D.-H., Lee, C.-W., Papp, J.K., Liu, Y.-S., Lun, Z., Clément, R.J., Shi, T., McCloskey, B.D., Guo, J., Balasubramanian, M., Ceder, G. Reversible Mn2+/Mn4+ double redox in lithium-excess cathode materials. *Nature*. 2018;556(7700):185-190.

[11] Lu, Z., MacNeil, D.D., Dahn, J.R. Layered Cathode Materials Li[Ni[sub x]Li[sub (1/3−2x/3)]Mn[sub (2/3−x/3)]]O[sub 2] for Lithium-Ion Batteries. *Electrochemical and Solid-State Letters*. 2001;4(11):A191.

[12] Hy, S., Liu, H., Zhang, M., Qian, D., Hwang, B.-J., Meng, Y.S. Performance and design considerations

for lithium excess layered oxide positive electrode materials for lithium ion batteries. *Energy Environ Sci*. 2016;9(6):1931-1954.

[13] Liu, H., Huang, J., Qian, D., Hy, S., Fang, C., Luo, J., Meng, Y.S. Communication—Enhancing the Electrochemical Performance of Lithium-Excess Layered Oxide Li1.13Ni0.3Mn0.57O2 via a Facile Nanoscale Surface Modification. *Journal of The Electrochemical Society*. 2016;163(6):A971-A973.

[14] Freire, M., Kosova, N.V., Jordy, C., Chateigner, D., Lebedev, O.I., Maignan, A., Pralong, V. A new active Li-Mn-O compound for high energy density Li-ion batteries. *Nat Mater*. 2016;15(2):173-177.

[15] Zheng, J., Gu, M., Xiao, J., Polzin, B.J., Yan, P., Chen, X., Wang, C., Zhang, J.-G. Functioning Mechanism of AlF3 Coating on the Li- and Mn-Rich Cathode Materials. *Chem Mater*. 2014;26(22):6320-6327.

[16] Zheng, J., Xu, P., Gu, M., Xiao, J., Browning, N.D., Yan, P., Wang, C., Zhang, J.-G. Structural and Chemical Evolution of Li- and Mn-Rich Layered Cathode Material. *Chem Mater*. 2015;27(4):1381-1390.

[17] Yan, P., Zheng, J., Tang, Z.-K., Devaraj, A., Chen, G., Amine, K., Zhang, J.-G., Liu, L.-M., Wang, C. Injection of oxygen vacancies in the bulk lattice of layered cathodes. *Nature Nanotechnology*. 2019;14(6):602-608.

[18] Rozier, P., Tarascon, J.M. Review—Li-Rich Layered Oxide Cathodes for Next-Generation Li-Ion Batteries: Chances and Challenges. *Journal of The Electrochemical Society*. 2015;162(14):A2490-A2499.

[19] Sathiya, M., Rousse, G., Ramesha, K., Laisa, C.P., Vezin, H., Sougrati, M.T., Doublet, M.L., Foix, D., Gonbeau, D., Walker, W., Prakash, A.S., Ben Hassine, M., Dupont, L., Tarascon, J.M. Reversible anionic redox chemistry in high-capacity layered-oxide electrodes. *Nature Materials*. 2013;12(9):827-835.

[20] Sathiya, M., Ramesha, K., Rousse, G., Foix, D., Gonbeau, D., Prakash, A.S., Doublet, M.L., Hemalatha, K., Tarascon, J.M. High Performance Li2Ru1-yMnyO3 (0.2 <= y <= 0.8) Cathode Materials for Rechargeable Lithium-Ion Batteries: Their Understanding. *Chem Mater*. 2013;25(7):1121-1131.

[21] Sathiya, M., Abakumov, A.M., Foix, D., Rousse, G., Ramesha, K., Saubanere, M., Doublet, M.L., Vezin, H., Laisa, C.P., Prakash, A.S., Gonbeau, D., VanTendeloo, G., Tarascon, J.M. Origin of voltage decay in high-capacity layered oxide electrodes. *Nature Materials*. 2015;14(2):230-238.

[22] McCalla, E., Abakumov, A.M., Saubanère, M., Foix, D., Berg, E.J., Rousse, G., Doublet, M.-L., Gonbeau, D., Novák, P., Van Tendeloo, G., Dominko, R., Tarascon, J.-M. Visualization of O-O peroxo-like dimers in high-capacity layered oxides for Li-ion batteries. *Science*. 2015;350(6267):1516.

[23] Pearce, P.E., Perez, A.J., Rousse, G., Saubanere, M., Batuk, D., Foix, D., McCalla, E., Abakumov, A.M., Van Tendeloo, G., Doublet, M.L., Tarascon, J.M. Evidence for anionic redox activity in a tridimensional-ordered Li-rich positive electrode beta-Li2IrO3. *Nat Mater*. 2017;16(5):580-586.

[24] Wang, X., Huang, W., Tao, S., Xie, H., Wu, C., Yu, Z., Su, X., Qi, J., Rehman, Z.u., Song, L., Zhang, G., Chu, W., Wei, S. Attainable high capacity in Li-excess Li-Ni-Ru-O rock-salt cathode for lithium ion battery. *J Power Sources*. 2017;359:270-276.

[25] Li, B., Shao, R., Yan, H., An, L., Zhang, B., Wei, H., Ma, J., Xia, D., Han, X. Understanding the Stability for Li-Rich Layered Oxide Li2RuO3Cathode. *Advanced Functional Materials*. 2016;26(9):1330-1337.

[26] Zheng, F., Zheng, S., Zhang, P., Zhang, X., Wu, S., Yang, Y., Zhu, Z.-z. Impact of Structural Transformation on Electrochemical Performances of Li-Rich Cathode Materials: The Case of Li2RuO3. *The Journal of Physical Chemistry C*. 2019;123(22):13491-13499.

[27] Li, X., Qiao, Y., Guo, S., Jiang, K., Ishida, M., Zhou, H. A New Type of Li-Rich Rock-Salt Oxide Li2Ni1/3Ru2/3O3 with Reversible Anionic Redox Chemistry. *Adv Mater*. 2019;31(11):1807825.

[28] Seo, D.H., Lee, J., Urban, A., Malik, R., Kang, S., Ceder, G. The structural and chemical origin of the oxygen redox activity in layered and cation-disordered Li-excess cathode materials. *Nat Chem*.

2016;8(7):692-697.

[29] Lee, J., Seo, D.-H., Balasubramanian, M., Twu, N., Li, X., Ceder, G. A new class of high capacity cation-disordered oxides for rechargeable lithium batteries: Li–Ni–Ti–Mo oxides. *Energy Environ Sci*. 2015;8(11):3255-3265.

[30] Lee, J., Urban, A., Li, X., Su, D., Hautier, G., Ceder, G. Unlocking the Potential of Cation-Disordered Oxides for Rechargeable Lithium Batteries. *Science*. 2014;343(6170):519-522.

[31] Yabuuchi, N., Nakayama, M., Takeuchi, M., Komaba, S., Hashimoto, Y., Mukai, T., Shiiba, H., Sato, K., Kobayashi, Y., Nakao, A., Yonemura, M., Yamanaka, K., Mitsuhara, K., Ohta, T. Origin of stabilization and destabilization in solid-state redox reaction of oxide ions for lithium-ion batteries. *Nat Commun*. 2016;7:13814.

[32] Yabuuchi, N., Takeuchi, M., Nakayama, M., Shiiba, H., Ogawa, M., Nakayama, K., Ohta, T., Endo, D., Ozaki, T., Inamasu, T., Sato, K., Komaba, S. High-capacity electrode materials for rechargeable lithium batteries: Li3NbO4-based system with cation-disordered rocksalt structure. *Proceedings of the National Academy of Sciences*. 2015;112(25):7650.

[33] Mohanty, D., Kalnaus, S., Meisner, R.A., Rhodes, K.J., Li, J., Payzant, E.A., Wood, D.L., Daniel, C. Structural transformation of a lithium-rich Li1.2Co0.1Mn0.55Ni0.15O2 cathode during high voltage cycling resolved by in situ X-ray diffraction. *J Power Sources*. 2013;229:239-248.

[34] Yan, H., Li, B., Yu, Z., Chu, W., Xia, D. First-Principles Study: Tuning the Redox Behavior of Lithium-Rich Layered Oxides by Chlorine Doping. *The Journal of Physical Chemistry C*. 2017;121(13):7155-7163.

[35] Laha, S., Morán, E., Sáez-Puche, R., Alario-Franco, M.Á., Dos santos-Garcia, A.J., Gonzalo, E., Kuhn, A., Natarajan, S., Gopalakrishnan, J., García-Alvarado, F. Li3MRuO5 (M = Co, Ni), new lithium-rich layered oxides related to LiCoO2: promising electrochemical performance for possible application as cathode materials in lithium ion batteries. *J Mater Chem A*. 2013;1(36):10686.

[36] An, K., Skorpenske, H.D., Stoica, A.D., Ma, D., Wang, X.L., Cakmak, E. First In Situ Lattice Strains Measurements Under Load at VULCAN. *Metall Mater Trans A*. 2011;42A(1):95-99.

[37] An, K. VDRIVE – Data reduction and interactive visualization software for event mode neutron diffraction. *ORNL Report, ORNL-TM-2012-621, Oak Ridge National Laboratory*. 2012.

[38] Larson, A.C., Dreele, R.B.V. General Structure Analysis System (GSAS). *Los Alamos National Laboratory Report (LAUR)*. 2004;86-748.

[39] Toby, B.H. EXPGUI, a graphical user interface for GSAS. *J Appl Crystallogr*. 2001;34:210-213.

[40] Momma, K., Izumi, F. VESTA: a three-dimensional visualization system for electronic and structural analysis. *Journal of Applied Crystallography*. 2008;41(3):653-658.

[41] YANG Tie-ying, W.W., YIN Guang-Zhi, LI Xiao-Long, GAO Mei, GU Yue-Liang, LI Li, LIU Yi, LIN He, ZHANG Xing-Min, ZHAO Bin, LIU Ting-Kun, YANG Ying-Guo, LI Zhong, ZHOU Xing-Tai, GAO Xing-Yu Introduction of the X-ray diffraction beamline of SSRF. *Nucl Sci Tech*. 2015;26((2)):020101.

[42] YU Hai-Sheng, W.X.-J., LI Jiong, GU Song-Qi, ZHANG Shuo,. The XAFS beamline of SSRF. *Nucl Sci Tech*. 2015;26(5):050102.

[43] Ravel, B., Newville, M. ATHENA, ARTEMIS, HEPHAESTUS: data analysis for X-ray absorption spectroscopy using IFEFFIT. *J Synchrotron Radiat*. 2005;12:537-541.

[44] Kresse, G., Joubert, D. From ultrasoft pseudopotentials to the projector augmented-wave method. *Physical Review B*. 1999;59(3):1758-1775.

[45] Kresse, G., Furthmüller, J. Efficient iterative schemes for ab initio total-energy calculations using a plane-wave basis set. *Physical Review B*. 1996;54(16):11169-11186.

[46] Kresse, G., Furthmüller, J. Efficiency of ab-initio total energy calculations for metals and

semiconductors using a plane-wave basis set. *Comp Mater Sci*. 1996;6(1):15-50.

[47] Perdew, J.P., Burke, K., Ernzerhof, M. Generalized Gradient Approximation Made Simple. *Phys Rev Lett*. 1996;77(18):3865-3868.

[48] Dudarev, S.L., Botton, G.A., Savrasov, S.Y., Humphreys, C.J., Sutton, A.P. Electron-energy-loss spectra and the structural stability of nickel oxide: An LSDA+U study. *Physical Review B*. 1998;57(3):1505-1509.

[49] Monkhorst, H.J., Pack, J.D. Special points for Brillouin-zone integrations. *Physical Review B*. 1976;13(12):5188-5192.

[50] Thackeray, M.M., Kang, S.H., Johnson, C.S., Vaughey, J.T., Benedek, R., Hackney, S.A. Li2MnO3-stabilized LiMO2 (M = Mn, Ni, Co) electrodes for lithium-ion batteries. *Journal of Materials Chemistry*. 2007;17(30):3112-3125.

[51] Zheng, S., Zhong, G., McDonald, M.J., Gong, Z., Liu, R., Wen, W., Yang, C., Yang, Y. Exploring the working mechanism of Li+ in O3-type NaLi0.1Ni0.35Mn0.55O2 cathode materials for rechargeable Na-ion batteries. *J Mater Chem A*. 2016;4(23):9054-9062.

[52] Chen, Y., Rangasamy, E., Liang, C., An, K. Origin of High Li+ Conduction in Doped Li7La3Zr2O12 Garnets. *Chem Mater*. 2015;27(16):5491-5494.

[53] Chen, Y., Cheng, Y., Li, J., Feygenson, M., Heller, W.T., Liang, C., An, K. Lattice-Cell Orientation Disorder in Complex Spinel Oxides. *Adv Energy Mater*. 2016;7(4):1601950.

[54] Liu, H., Chen, Y., Hy, S., An, K., Venkatachalam, S., Qian, D., Zhang, M., Meng, Y.S. Operando Lithium Dynamics in the Li-Rich Layered Oxide Cathode Material via Neutron Diffraction. *Adv Energy Mater*. 2016;6(7):1502143.

[55] Liu, H., Liu, H., Seymour, I.D., Chernova, N., Wiaderek, K.M., Trease, N.M., Hy, S., Chen, Y., An, K., Zhang, M., Borkiewicz, O.J., Lapidus, S.H., Qiu, B., Xia, Y., Liu, Z., Chupas, P.J., Chapman, K.W., Whittingham, M.S., Grey, C.P., Meng, Y.S. Identifying the chemical and structural irreversibility in LiNi0.8Co0.15Al0.05O2 – a model compound for classical layered intercalation. *J Mater Chem A*. 2018;6(9):4189-4198.

[56] Cava, R.J., Murphy, D.W., Zahurak, S., Santoro, A., Roth, R.S. The Crystal-Structures of the Lithium-Inserted Metal-Oxides Li0.5tio2 Anatase, Liti2o4 Spinel, and Li2ti2o4. *J Solid State Chem*. 1984;53(1):64-75.

[57] Cai, L., Liu, Z., An, K., Liang, C. Unraveling structural evolution of LiNi0.5Mn1.5O4 by in situ neutron diffraction. *J Mater Chem A*. 2013;1(23):6908-6914.

[58] Oikawa, K., Kamiyama, T., Izumi, F., Nakazato, D., Ikuta, H., Wakihara, M. Neutron and X-Ray Powder Diffraction Studies of LiMn2−yCryO4. *J Solid State Chem*. 1999;146(2):322-328.

[59] Satish, R., Lim, K., Bucher, N., Hartung, S., Aravindan, V., Franklin, J., Lee, J.-S., Toney, M.F., Madhavi, S. Exploring the influence of iron substitution in lithium rich layered oxides Li2Ru1-xFexO3: triggering the anionic redox reaction. *J Mater Chem A*. 2017;5(27):14387-14396.

[60] Lyu, Y., Hu, E., Xiao, D., Wang, Y., Yu, X., Xu, G., Ehrlich, S.N., Amine, K., Gu, L., Yang, X.-Q., Li, H. Correlations between Transition-Metal Chemistry, Local Structure, and Global Structure in Li2Ru0.5Mn0.5O3 Investigated in a Wide Voltage Window. *Chem Mater*. 2017;29(21):9053-9065.

[61] Hu, E.Y., Lyu, Y.C., Xin, H.L.L., Liu, J., Han, L.L., Bak, S.M., Bai, J.M., Yu, X.Q., Li, H., Yang, X.Q. Explore the Effects of Microstructural Defects on Voltage Fade of Li- and Mn-Rich Cathodes. *Nano Lett*. 2016;16(10):5999-6007.

[62] Johnson, C.S., Kim, J.-S., Jeremy Kropf, A., Kahaian, A.J., Vaughey, J.T., Thackeray, M.M. The role of Li2MO2 structures (M=metal ion) in the electrochemistry of (x)LiMn0.5Ni0.5O2·(1−x)Li2TiO3 electrodes

for lithium-ion batteries. *Electrochem Commun*. 2002;4(6):492-498.

[63] Hirano, A., Kanno, R., Kawamoto, Y., Takeda, Y., Yamaura, K., Takano, M., Ohyama, K., Ohashi, M., Yamaguchi, Y. Relationship between non-stoichiometry and physical properties in LiNiO2. *Solid State Ionics*. 1995;78(1):123-131.

[64] Lu, Z., Dahn, J.R. Understanding the Anomalous Capacity of Li/Li[Ni[sub x]Li[sub (1/3−2x/3)]Mn[sub (2/3−x/3)]]O[sub 2] Cells Using In Situ X-Ray Diffraction and Electrochemical Studies. *Journal of The Electrochemical Society*. 2002;149(7):A815.

[65] Grey, C.P., Dupré, N. NMR Studies of Cathode Materials for Lithium-Ion Rechargeable Batteries. *Chem Rev*. 2004;104(10):4493-4512.

[66] Zheng, X., Li, X., Wang, Z., Guo, H., Huang, Z., Yan, G., Wang, D. Investigation and improvement on the electrochemical performance and storage characteristics of LiNiO 2 -based materials for lithium ion battery. *Electrochimica Acta*. 2016;191:832-840.

[67] Meng, K., Wang, Z., Guo, H., Li, X., Wang, D. Improving the cycling performance of LiNi 0.8 Co 0.1 Mn 0.1 O 2 by surface coating with Li 2 TiO 3. *Electrochimica Acta*. 2016;211:822-831.

[68] Dupin, J.-C., Gonbeau, D., Vinatier, P., Levasseur, A. Systematic XPS studies of metal oxides, hydroxides and peroxides. *Phys Chem Chem Phys*. 2000;2(6):1319-1324.

[69] Hong, J., Lim, H.-D., Lee, M., Kim, S.-W., Kim, H., Oh, S.-T., Chung, G.-C., Kang, K. Critical Role of Oxygen Evolved from Layered Li–Excess Metal Oxides in Lithium Rechargeable Batteries. *Chem Mater*. 2012;24(14):2692-2697.

[70] Xie, Y., Saubanère, M., Doublet, M.L. Requirements for reversible extra-capacity in Li-rich layered oxides for Li-ion batteries. *Energ Environ Sci*. 2017;10(1):266-274.

Graphic for manuscript

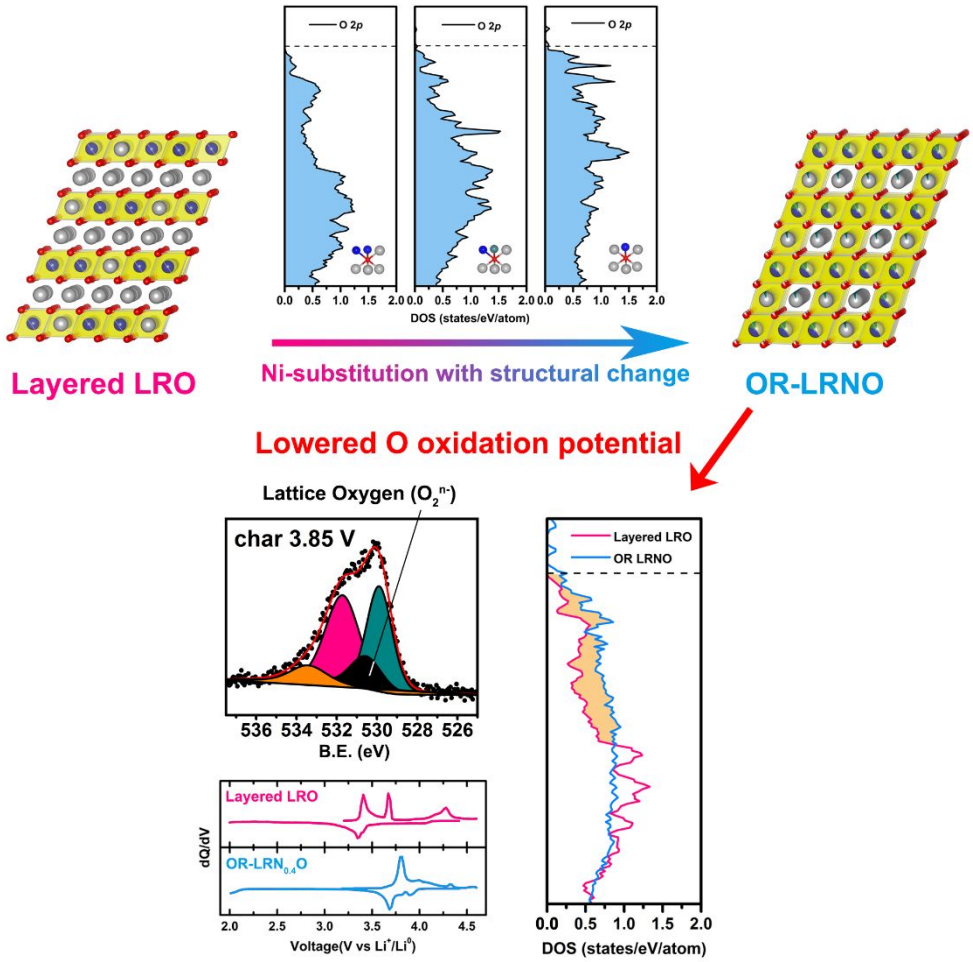
O 2p
O 2p
O 2p
0.0 0.5 1.0 1.5 2.0
DOS (states/eV/atom)
Layered LRO
Ni-substitution with structural change
OR-LRNO
Lowered O oxidation potential
Lattice Oxygen (O_2^{n-})
char 3.85 V
536 534 532 530 528 526
B.E. (eV)
Layered LRO
OR-LRN$_{0.4}$O
dQ/dV
2.0 2.5 3.0 3.5 4.0 4.5
Voltage(V vs Li^+/Li^0)
Layered LRO
OR LRNO
0.0 0.5 1.0 1.5 2.0
DOS (states/eV/atom)